Temperature field around underground power cable for dry and saturated conditions under static and cyclic thermal loads

Shahbaz Ahmad
Kiel University: Christian-Albrechts-Universitat zu Kiel
Zarghaam Haider Rizvi (zarghaam.rizvi@ifg.uni-kiel.de)
Christian Albrechts Universitat zu Kiel https://orcid.org/0000-0002-7553-8310
Joscha Loose
University of Kiel: Christian-Albrechts-Universitat zu Kiel
Frank Wuttke
Kiel University: Christian-Albrechts-Universitat zu Kiel
Vineet Tirth
King Khalid University College of Engineering
Saiful Islam
King Khalid University College of Engineering

Research Article

Keywords: Underground Power Cables, Energy Geotechnics, Cyclic Thermal Loading, Natural Convection, Thermal Charging

Posted Date: June 1st, 2021

DOI: https://doi.org/10.21203/rs.3.rs-472964/v1

Heat & Mass Transfer manuscript No.
(will be inserted by the editor)

Temperature field around underground power cable for dry and saturated conditions under static and cyclic thermal loads

Shahbaz Ahmad1 · Zarghaam Haider Rizvi12 · Joscha Loose1 · Frank Wuttke1 · Vineet Tirth3,4 · Saiful Islam5

Received: date / Accepted: date

Abstract The safe operation of underground power cables is limited by the temperature of insulation around the conductor which heats up due to joule heating. The insulation temperature depends on the seasonal and diurnal power demand and variations in the surrounding soil's moisture content. The previous scientific investigations are limited to theoretical and numerical analyses for cyclic loads and experimental studies for only dry conditions with static thermal loads. In this study, a series of large-scale laboratory tests are performed for static and cyclic thermal loads with dry and saturated sand. The cyclic thermal loads with symmetrical and unsymmetrical heating-cooling times are done with dry sand, which is the worst-case scenario for heat dissipation. The cyclic thermal loading on dry sand shows strong thermal charging and is higher with a shorter relaxation time. The static thermal loading results show a significant improvement in the heat dissipation ability with saturated sand due to higher thermal conductivity. However, the heat transfer with saturated sand suggests a strong convection cell formation after three days of heating above the heater. The channelisation of heat with convection cell sand facilitates cooling but is not desirable for power cables below crop fields.

Keywords Underground Power Cables · Energy Geotechnics · Cyclic Thermal Loading · Natural Convection · Thermal Charging

1 Introduction

Power transmission and distribution play an essential role in energy security and industrial growth of a nation. Power transmission over a long distance is done by high voltage transmission lines which are prone to high winds, snow and ice storms, earthquakes and metal wire theft (1)(2). The other issue with the overhead line is high electromagnetic pollution (hiss or hum noises)(3). The adoption of power generation from decentralised green systems such as wind, solar and tidal from favourable generation sites, and the transmission to industrial consumption centres with high voltage overhead lines would render a large area unusable(4). Therefore, in the past decades, intensive research has been done to improve the understanding and enhance the knowledge about heat and mass movement around the Under Ground Powercable System (UGPS). The limiting factor in a UGPS is the melting temperature of cross-linkable polyethene (XLPE) around the conductor which heats up due to resistance to electric current flow (Joule heating)(5)(6)(7). Thus, means and methods have been applied to dissipate the generated heat into

1Geomechanics & Geotechnics
Kiel University, Kiel, Germany
E-mail: zarghaam.rizvi@ifg.uni-kiel.de

2GeoAnalysis Engineering GmbH
Kiel, Germany
E-mail: zarghaam.rizvi@geoanalysis-engineering.de

3Mechanical Engineering Department,
College of Engineering, King Khalid University,
Abha 61411, Asir, Kingdom of Saudi Arabia

4Research Center for Advanced Materials Science (RCAMS)
King Khalid University, Guraiger
Abha-61413, Asir, Kingdom of Saudi Arabia

5 Civil Engineering Department,
College of Engineering, King Khalid University,
Abha 61411, Asir, Kingdom of Saudi Arabia

the surrounding soils efficiently to improve the current carrying capacity (ampacity) of the UGPS by an optimised arrangement of the cables, (8)(9)(10)(11)(12) and if required replacing the native soil by the trench backfill materials(13)(14)(15) (16).

The first assumption for all theoretical and experimental studies, and code of practice of International Electrotechnical Commission (IEC)(6) for the UGPS is that the cable and the surrounding soil attain a static equilibrium and result in an isotherm around the cables. The second assumption arises from the Joule heating of the UPGS that results in moisture migration from soil in the vicinity of the cable. The dry soil around the UGPS is the worst-case scenario as it reduces the thermal conductivity and results in ”hot spot” formation. Therefore, most studies are limited to static thermal loading and with dry soil. However, the validity of both assumptions is challenged for high voltage (above 345kV) UGPS to transport energy generated from green sources. The transported power in UGPS from green sources fluctuates every day due to variable wind speed, cloud cover and local weather conditions, and variation in nominal and peak demand load hours for hot and cold seasons. Also, the degree of saturation, the most influencing parameter for the thermal conductivity value of soil, varies with diurnal and seasonal precipitation and evapotranspiration.

Therefore, recent numerical (17) and theoretical(18) studies have started considering dynamic influences. The studies showed the effect of daily load cycles on the UGPS . The results show that cables could carry more power with proper dynamic thermal analysis. However, no experimental tests are reported in the literature of cyclic thermal loading and comparative behaviour of dry and saturated conditions around the UGPS. The experimental programs to study the distributions of temperature and moisture fields around the UGPS are done both at field and laboratory scales(19). The field-scale experiments offer a rich data set of the real-world boundary and environmental conditions but are challenging to set up and resource-intensive(20). The substantial effort is the work by Snijders et al.(21), where for the first time the field measurements have been reported. In recent work, the field measurements are also presented by Trinks(22) for different soil and surrounding conditions around a 110 kV cable. Ainhirn (23) presented the field measurements of UGPS, and sensitivity analysis is done for various environmental and material parameters. The study showed that surrounding soil temperature and thermal conductivity have the most decisive influence on the cable temperature and control the ampacity.

The field-scale experiments lack fine control on the boundary conditions and material heterogeneity, which are omnipresent, influencing the measured temperature and moisture fields (24). The small number of data sets available from field-scale experiments with many variables render the results limited in scope and proper understanding of the involved physics. Therefore, medium and large-scale laboratory tests have gained more importance where process controlling parameters are regulated in a better fashion for an adequate understanding of the physical phenomenon (25) (26). The medium-scale rectangular box fitted with a cylindrical heating source and temperature and moisture measuring sensors has gained popularity among researchers due to ease of workability, and a decent test setup cost(27). Using the same setup, Vollaro et al. (24) studied the effect of non-homogeneous soil and backfill (11) around a heated cylinder with a static loading scheme. Salata et al. (15) have provided experimental evidence showing underestimation of the temperature field around a power cable using the IEC method, and a modification to the method is suggested with a correction coefficient derived from experiments(28). The medium-scale experiments offer a good insight into temperature and moisture fields' development with changing heating and boundary conditions. However, the effect of the boundary conditions and accumulation of generated heat in the surrounding soil mass due to limited size resulted in a higher temperature field close to the heater, and excess moisture near the boundaries (20). Therefore, large scale boxes fitted with single(4) and multiple heaters(29) are built to eliminate the boundary effect and have good heat dissipation characteristics.

In this paper, we present an extensive experimental study with symmetric and unsymmetrical thermal heating to provide the surrounding soil's behaviour under static and cyclic thermal loading. Also, a comparative study of dry and saturated sand is performed with five days of static heating, and results are presented in the form of graphs and thermal contour plots. The results provide a fundamental understanding of the dynamic equilibrium and formation of convection cells in the thermal loaded saturated sand and could be used to benchmark numerical models for such studies.

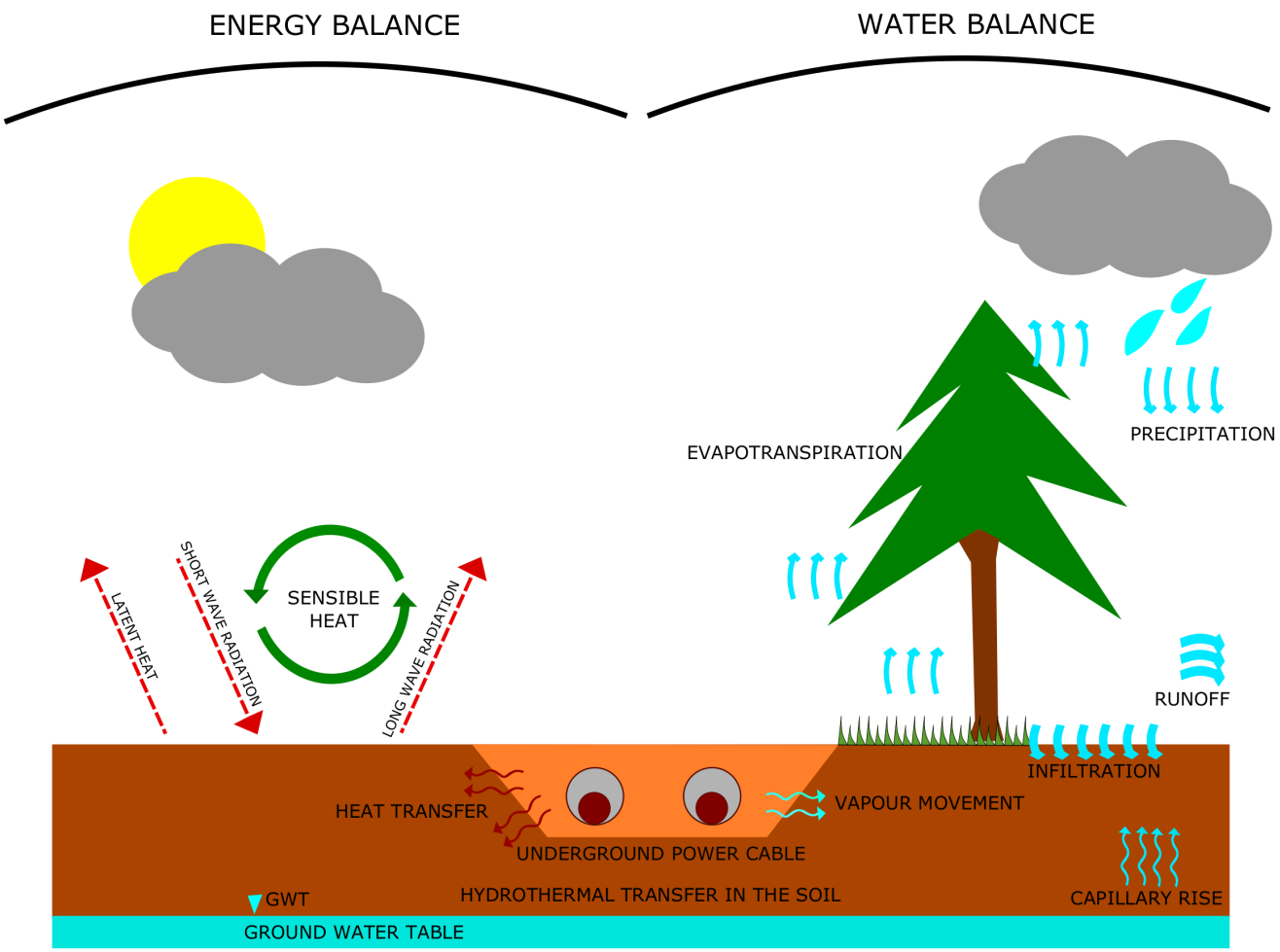

Fig. 1: Interaction of UGPS with environmental and surrounding conditions and different modes of heat and mass transfer into the surrounding soil mass.

Nomenclature

a volumetric air content
c, C_p specific heat $[Jkg^{-1}K^{-1}]$
C volumetric heat capacity $[Jm^{-3}K^{-1}]$
D diffusion coefficient of water vapour in air $[m^2s^{-1}]$
D_T macroscopic diffusivity for moisture transport due to $\nabla T [m^2s^{-1}K^{-1}]$
D_θ macroscopic diffusivity for moisture transport due to $\nabla\theta_l [m^2s^{-1}]$
e empirical factor
g acceleration due to gravity $[ms^{-2}]$
h relative humidity
H specific enthalpy $[JKg^{-1}]$
k unit vector in the z-direction
K hydraulic conductivity $[ms^{-1}]$
L latent heat of evaporation $[JKg^{-1}]$
M molar mass $[Kgmol^{-1}]$
p_v partial pressure of water vapour [Pa]
P total gas pressure [Pa]
q flux density for mass $[Kgm^{-2}s^{-1}]$
q_h flux density for heat $[Jm^{-2}s^{-1}]$

R universal gas constant [$\mathrm{Jmol^{-1}K^{-1}}$]
S porosity
t time [s]
T temperature [K]
x,y horizontal coordinate [m]
z vertical coordinate, positive downward [m]

Greek Symbols
ε low value of θ_l
$\zeta(\nabla\,\mathrm{T})_\mathrm{a}/\nabla\,\mathrm{T}$
θ volumetric moisture content
λ Effective thermal conductivity [$\mathrm{W\,m^{-1}K^{-1}}$]
ψ moisture potential [m]
ρ density [$\mathrm{kgm^{-3}}$]

Subscripts
0 reference value
a air
d drying
h heat
k critical
l liquid
m moisture
r reversal
s saturation
v vapour
w wetting

2 Theory of coupled heat and mass transport in sand

The theoretical and numerical study of heat and mass transfer around the UGPS is based on the rudimentary static equilibrium and isotherm assumption. However, the heat and mass transfer in porous media such as soil are comprised of complex interactions among gas, heat, liquid water and vapour flow. A detailed study of heat and mass transfer in sand based on the thermodynamics of irreversible process is presented (30). The agreement between theory and experiment was only partial and required many assumptions. The other approach is the 'mechanistic' explanation of the process and is used for many porous media due to simplicity of the computation of diffusion parameters (31). The theory has limitations such as the moisture potential's hysteresis relation, and the moisture content not being taken into account. Also, the solid matrix's deformation is not allowed, and the porous medium must be homogeneous and isotropic in a macroscopic sense. The phase change phenomena of boiling, freezing and thawing are not included. The Knudsen effect in the gas phase and the surface phenomena at the interface between the matrix and the liquid are not considered. The following simplifications are also applied for the formulation of the governing coupled partial differential equations. For fluids in the porous media, the solutes are assumed to be absent; thus, the liquid phase is pure water, and the movement is driven by viscous flow under the influence of capillary and adsorptive forces. Similarly, the vapour movement is by diffusion in the gas-filled pores with air as an inert gas, and the free convection in the gas phase is neglected. In the case of heat transfer, the radiation effect is negligible, and the assumption of local thermodynamic equilibrium among the liquid in contact with its vapour holds. Also, the total pressure is assumed uniform and constant, and the temperature dependence of physical constants is neglected (32). With these limitations and assumptions, the mass balance in the porous media is given as

The liquid flux density

$$\mathrm{q_l} = -\rho_\mathrm{l}(\mathrm{D}_{\theta\mathrm{l}}\nabla\theta_\mathrm{l} + \mathrm{D}_{\mathrm{Tl}}\nabla\mathrm{T} + \mathrm{K}\mathbf{k}) \tag{1}$$

where, $\mathrm{D_{Tl}}$ and $\mathrm{D}_{\theta\mathrm{l}}$ are the thermal liquid and isothermal diffusivities respectively

$$\mathrm{D}_{\theta\mathrm{l}} = K\partial\psi/\partial\theta_\mathrm{l}, \mathrm{D}_{\mathrm{Tl}} = K\partial\psi/\partial\mathrm{T} \tag{2}$$

The total water vapour flux is the summation of the isothermal flux component and the temperature-driven flux component

$$\mathbf{q}_\mathrm{v} = -\rho_\mathrm{l}(\mathrm{D}_{\theta\mathrm{v}}\nabla\theta_\mathrm{l} + \mathrm{D}_{\mathrm{Tv}}\nabla\mathrm{T}) \tag{3}$$

$$\mathrm{D}\theta_\mathrm{v} = \mathrm{f(a)D}\frac{\mathrm{P}}{\mathrm{P}-\mathrm{p_v}}\frac{\mathrm{Mg}}{\mathrm{RT}}\frac{\rho_\mathrm{v}}{\rho_\mathrm{l}}\frac{\partial\psi}{\partial\theta_\mathrm{l}} \tag{4}$$

$$\mathrm{D}_{\mathrm{Tv}} = \mathrm{f(a)D}\frac{\mathrm{P}}{\mathrm{P}-\mathrm{p_v}}\frac{\rho_\mathrm{v}}{\rho_\mathrm{l}}\frac{\zeta}{\mathrm{p_{vs}}}\frac{\mathrm{dp_{vs}}}{\mathrm{dT}} \tag{5}$$

The partial pressure of water vapour is related to the soil water potential through the fractional relative humidity as

$$\mathbf{p}_\mathrm{v} = \mathrm{hp_{vs}} = \mathrm{p_{vs}}\exp(\mathrm{Mg}\psi/\mathrm{RT}) \tag{6}$$

$$\mathrm{f(a)} = \mathrm{a}+\theta_\mathrm{l} = \mathrm{S}, \quad \text{for} \quad \theta_\mathrm{l} \le \theta_\mathrm{lk} \quad \mathrm{f(a)} = \mathrm{a}+\mathrm{a(S-a)/(S-}\theta_\mathrm{lk}), \quad \text{for} \quad \theta_\mathrm{l} > \theta_\mathrm{lk} \tag{7}$$

$$\zeta = (\nabla\mathrm{T})_\mathrm{a}/\nabla\mathrm{T}) \tag{8}$$

The total moisture flux is the combination of liquid and vapour fluxes

$$\mathbf{q_m} = \mathbf{q_l} + \mathbf{q_v} = -\rho_\mathrm{l}(\mathrm{D}_\theta\nabla\theta_\mathrm{l} + \mathrm{D_T}\nabla\mathrm{T} + \mathbf{Kk}) \tag{9}$$

Similarly, the total energy transport in the porous media is the summation of sensible, convective and latent heat fluxes

$$\mathbf{q_h} = -\lambda\nabla\mathrm{T} + \mathrm{c_1(T-T_0)}\mathbf{q}_\mathrm{m} - \mathrm{L}\rho_1\mathrm{D}_{\theta\mathrm{v}}\nabla\theta_\mathrm{l} \tag{10}$$

The transport equations described above for liquid water, heat and water vapour are combined to obtain a coupled system of two partial differential equations, with temperature T and volumetric moisture content θ_l,

$$\left\{1 + \frac{(\mathrm{S}-\theta_\mathrm{l})\rho_\mathrm{v}}{\rho_\mathrm{l}}\frac{\mathrm{Mg}}{\mathrm{RT}}\frac{\partial\psi_\mathrm{l}}{\partial\theta} - \frac{\rho_\mathrm{v}}{\rho_\mathrm{l}}\right\}\frac{\partial\theta_\mathrm{l}}{\partial_\mathrm{t}} + \frac{(\mathrm{S}-\theta_1)\mathrm{h}}{\rho_\mathrm{l}}\frac{\mathrm{d}\rho_\mathrm{vs}}{\mathrm{dT}}\frac{\partial\mathrm{T}}{\partial\mathrm{t}} = \nabla(\mathrm{D}_\theta\nabla\theta_\mathrm{l}) + \nabla(\mathrm{D_T}\nabla\mathrm{T}) + \partial\mathbf{K}/\partial\mathrm{z} \tag{11}$$

$$\begin{aligned}\left\{\frac{\mathrm{L(S}-\theta_\mathrm{l})\rho_\mathrm{v}\mathrm{Mg}}{\mathrm{RT}}\frac{\partial\psi}{\partial\theta_\mathrm{l}} - \mathrm{L}\rho_\mathrm{v}\right\}\frac{\partial\theta_\mathrm{l}}{\partial\mathrm{t}} + \left\{\mathrm{C} + \mathrm{L(S}-\theta_\mathrm{l})\mathrm{h}\frac{\mathrm{d}\rho_\mathrm{vs}}{\mathrm{dT}}\right\}\frac{\partial\mathrm{T}}{\partial\mathrm{t}} &= \nabla(\lambda\nabla\mathrm{T}) + \mathrm{L}\rho_\mathrm{l}\nabla(\mathrm{D}_{\theta\mathrm{v}}\nabla\theta_\mathrm{l}) \\ &\quad - \mathrm{c_l}(\mathrm{q_l}\nabla\mathrm{T}) - \mathrm{c_{pv}}(\mathrm{q_v}\nabla\mathrm{T})\end{aligned} \tag{12}$$

The above two equations are solved with the finite element (33) and finite difference (34) methods for atmospheric boundary conditions for the UGPS to compute temperature and moisture fields. However, the "mechanistic" formulated equations offer large errors at low and high moisture values and with rapidly changing saturation level. Therefore, for an accurate estimation for such a complex problem of the temperature field around a heater, experimental studies are ideal and are done here.

3 Material and Method

The large scale testing box is fabricated with holding staffs for the heater. The plate is mounted on wooden beams to avoid direct contact with the surface. The sides are constructed with a sturdy C section able to hold the load coming from the filled, compacted sand.The cylindrical heater is fastened with bolt mechanism and with the ends of the heater insulated with a nylon block to prevent heat loss (Fig. 3a.). The side boundaries are made with transparent plexiglass that allows for observation of the progress and is a good insulator. The sand for the test is collected from a site near Kiel, Germany and the chemical and thermo-physical properties are given below in Table 1 and 2. A short description of the experiment assembly is given here, and the detail can be found in Ahmad et al.(4).

3.1 Sand

The X-ray fluorescence (XRF) analysis of sand reveals the primary composition of silica with other chemicals in trace amounts (Table 1). The thermophysical material properties of the sand are given in Table 2. The geotechnical laboratory tests show that the sand is uniform sand with a porosity of 0.36. The thermal conductivity in dry and full saturation is 0.365 and 2.54 $\mathrm{Wm^{-1}K^{-1}}$.

Table 1: XRD results for the sand

Weight Percent Oxides of the soil sample						
Compound	SiO_2	Al_2O_3	Fe_2O_3	CaO	MgO	K_2O
Percentage	99.27819	0.193343	0.078948	0.04028	0.098282	0.019334

Table 2: Thermo-Physical properties of Sand

Properties	Values
Gravel, >2 mm (wt.%)	4.78
Sand, 0.063-2 mm (wt.%)	95.16
Silt and Clay, <0.063 mm (wt.%)	0.06
Porosity n (-)	0.36
Solids specific gravity G_s (-)	2.66
Dry Density ρ_d (Kgm^{-3})	1720
Grain diameter at 10% passing D_{10} (mm)	0.27
Grain diameter at 50% passing D_{50} (mm)	0.60
Coefficient of uniformity C_u (-)	2.63
Coefficient of curvature C_c (-)	0.88
Dry effective thermal conductivity λ_{dry} $(Wm^{-1}K^{-1})^1$	0.365
Saturated eff. thermal conductivity λ_{sat} $(Wm^{-1}K^{-1})^1$	2.54
Dry effective specific heat capacity c_{dry} $(MJm^{-3}K^{-1})^1$	1.39
Saturated eff. specific heat capacity c_{sat} $(MJm^{-3}K^{-1})^1$	2.453
Unified soil classification system (USCS)	SP[2]

[1] Effective parameters obtained using Decagon KD2 Pro transient thermal needle probes, [2] Poorly graded sand

3.2 Experimental setup

The rectangular box for the test is 1800 mm long, 1000 mm wide and 1200 mm high (see Fig 2 (a)). The experimental setup is the same as in Ahmad et al. (4) with minor changes in the data acquisition setup to study relaxation time and to deal with saturated conditions. The fabricated container had Plexiglas faces on all the four sides for precise observation which were bevelled on the edges and top to ensure safety for the working personnel. The container was secluded directly from the ground using solid wooden planks and rubber sheets to remove any hindrance and minimise heat loss.

The sand was placed inside the tank in a layered manner (10 cm each) to ensure proper compaction of each layer. Also, at the same time maintaining the respective positions of the thermocouples. For compaction, a wooden tamping bar was used and overall density of $1.65\ gcm^{-3}$ has been achieved to avoid settlement during saturation. To implement the saturation condition, a bottom to top approach was used. Four flexible rubber pipes at each corner were used, which run to the container's bottom. In this process, the sand is saturated from bottom to top, thereby removing the trapped air from the inter-granular pores. Commercially available water sealant was used to avoid any leakage from the container. After the container was filled up to the top, it was covered with thin, flexible aluminium sheets to avoid heat decampment. A drainage outlet was also provided.

3.3 Thermocouples and Heater

The UGPS was simulated with a heater rod systematically devised with an electrical heater inside it. The heater rod (80 cm long, external diameter 5cm) was placed firmly inside the container between two upright stands, and fixed between two supports (5cm wide each). It was placed along the short edge (100 cm wide side), with its centre at a distance of 75cm from the bottom of the container. The schematic diagram of the heater rod is shown in Fig 3 (a). The temperatures and moisture data are recorded with National Instruments thermocouples and 15 cm long three pin TDRs. 32 K type thermocouples (TCs) along with 8 TDRs were set up at definite locations inside the box with distances measured from the surface of the heater rod (see Fig 2 (a)). The TCs had an operating temperature range of –55 °C to 550°C. The accuracy of the heating system is provided by the manufacturer with ± 0.5 K and is cross-validated before installation. The K-type thermocouples bought from National Instruments showed a deviation smaller than ± 0.3 K when tested against the resistance temperature detectors (RTDs) Pt-100 sensors.

Furthermore, a separate test to evaluate the sensors was conducted with water filled in the box also fitted with 4 Pt-100 sensors. All thermocouples and the RTDs in water inside the box were within a range of 0.25K, which is well within the permissible error range. Ambient temperatures were measured using two TC's placed outside of the box. Four thermocouples are placed on the heater's circumference, and the aluminium foil is wrapped to give uniform heat distribution from the cable. The average value of these four sensors is plotted as heater temperature in both static and dynamic thermal loading scenarios. Table 3 enlists the respective distances of the attached TCs.

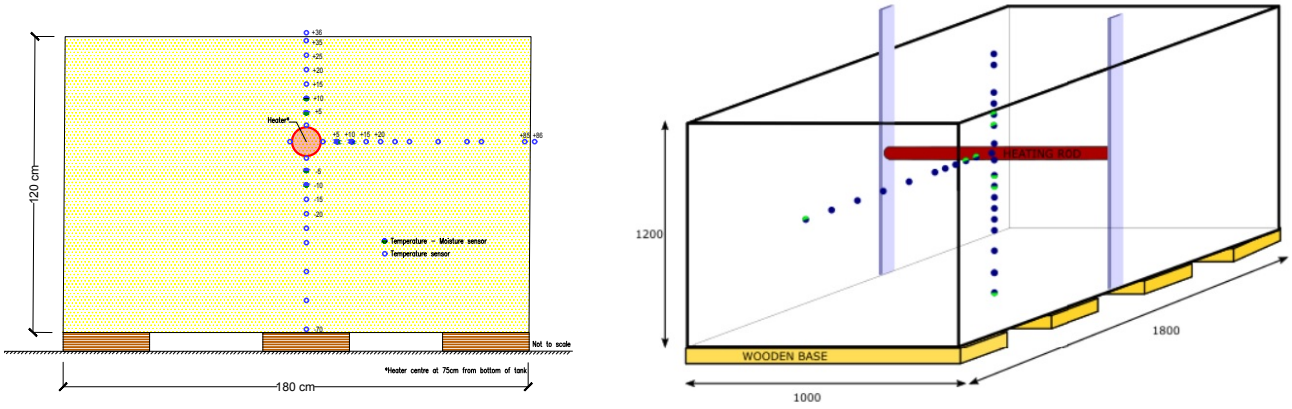

Fig. 2: The arrangement of heater, thermocouples and the box a) schematic showing the location of 32 thermocouples in vertical and horizontal planes at the middle section. b) The three dimensional schematic of box, thermocouple and the heater with holding staff .

Table 3: Distance and position of the Thermocouples

Position of the Thermocouples	Name and Respective Distances[1]
Heater Surface	A24, A10, A30, A31
Outside Container	A0 (86), A8(40)
Above Heater	A7 (5), A11 (10), A14 (15), A26 (20), A9 (25), A27 (30)
Below Heater	A20 (5), A4 (10), A2 (15), A1 (20), A3 (25), A19 (30), A15(40), A12 (50), A25 (70)
Horizontal Direction	A18 (5), A21 (10), A17 (15), A5 (20), A16 (25), A6 (30), A28(40), A22 (50), A23 (55), A13 (85)

[1] (in cm from the surface of heater rod and distance mentioned in the parenthesis)

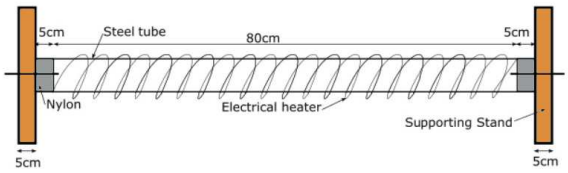

(a) The heating rod

(b) The laboratory set up of box with sand

Fig. 3: a) The schematic diagram of the heating rod with the holding staffs. b) The large scale box with sand during measurement.

4 Results and Discussion

The dynamic thermal loading test with only dry sand and static thermal loading test with both dry and saturated sand are performed. The dynamic loadings are performed with three separate loadings of the equispaced heating-cooling, the shorter heating and longer cooling and the thermal relaxation time. The static thermal loading tests with dry and saturated sand are done to assess the longterm behaviour of the UGPS. The results are arranged in two separate subsections: the dynamic thermal loading with dry sand and the static thermal loading with dry and saturated sand.

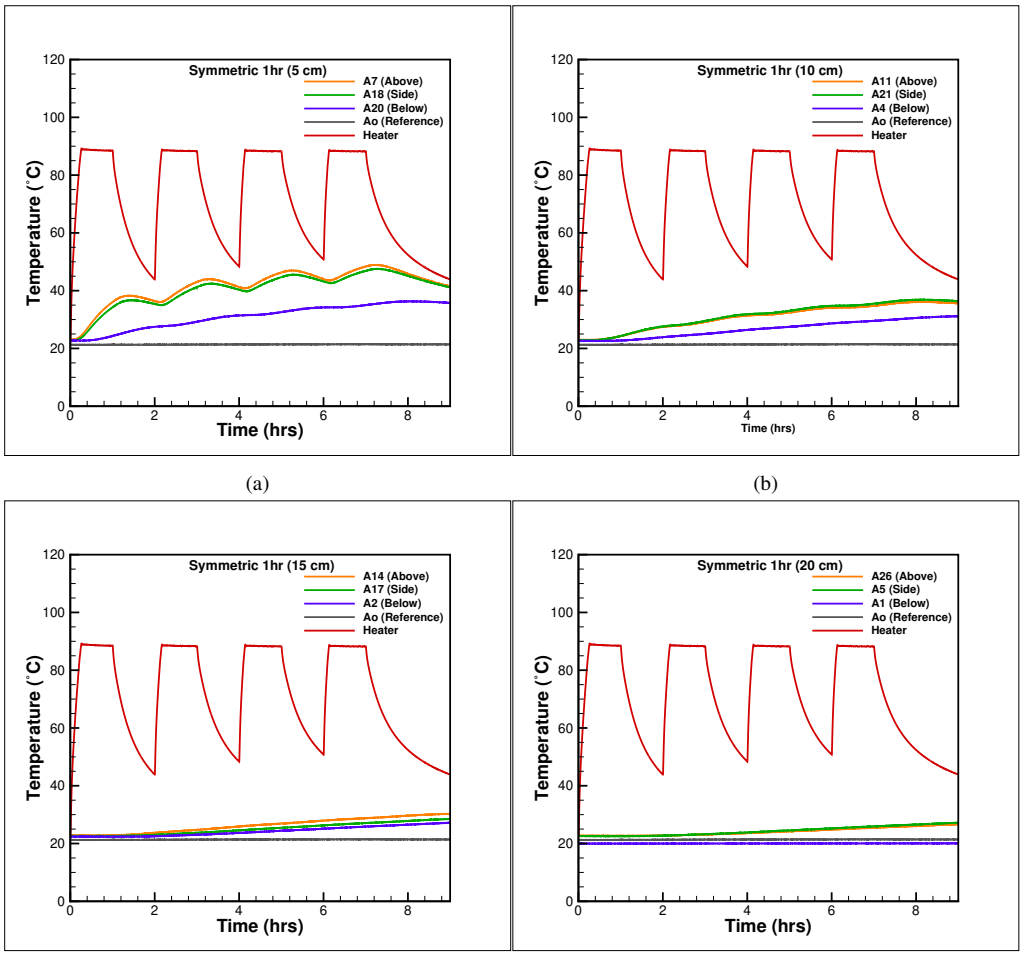

Fig. 4: The symmetrical heating-cooling cycle of 1 hour at a)5cm b)10cm c)15cm d)20cm from the heater surface.

4.1 The dynamic thermal loading with dry sand

The thermal cyclic (symmetrical and unsymmetrical heating) and relaxation time tests are performed with dry sand with a maximum heater temperature of 70°C. All the tests are performed at surrounding temperature close to 20 °C.

4.1.1 Symmetrical thermal heating-cooling cycles

Two tests are performed with equal heating and cooling cycles of 1 hour and 12 hours, as shown in Figure 4 and 5. For both tests, it is observed that the heater's operational effect is felt at all the TCs instantaneously. The 1-hour test also shows that the cooling time is insufficient to bring the system to the original state (Fig. 4a-d), causing a gradual increasing in the temperature of sand throughout the box. The effect of heating is felt at all the observation points ranging between 5-20 cm from the heater´s outer surface. The maximum influence is noticed at the TCs above the heater at 5cm distance where the temperature reaches a value of 48.92 °C. The minimum temperature of 26.69 °C is recorded below the heater. The observation suggests a permanent thermal charging of the system and is not desirable for the UGPS. The excess temperature reduces the thermal gradient between the heater and its surrounding and thus promotes heat storage and drying.

For 12 hours of heating-cooling cycles, the thermal charging effect is less significant. However, the intensity of charging is different from the 1-hour cycles. After the first cycle for TC at 5cm above the heater, a maximum temperature of 47.73 °C is recorded, which increases to 51.65 °C after five heating cycles. A similar trend is observed at the furthest TC at 20 cm from the heater, but the charging effect is pacified (Fig. 5d).

In both experiments, it is evident that symmetrical heating-cooling cycles do not offer sufficient time for the surrounding sand to dissipate the extra heat given off by the heater. Therefore, the unsymmetrical heating-cooling experimental tests are performed to observe improvement in cooling of heated sand.

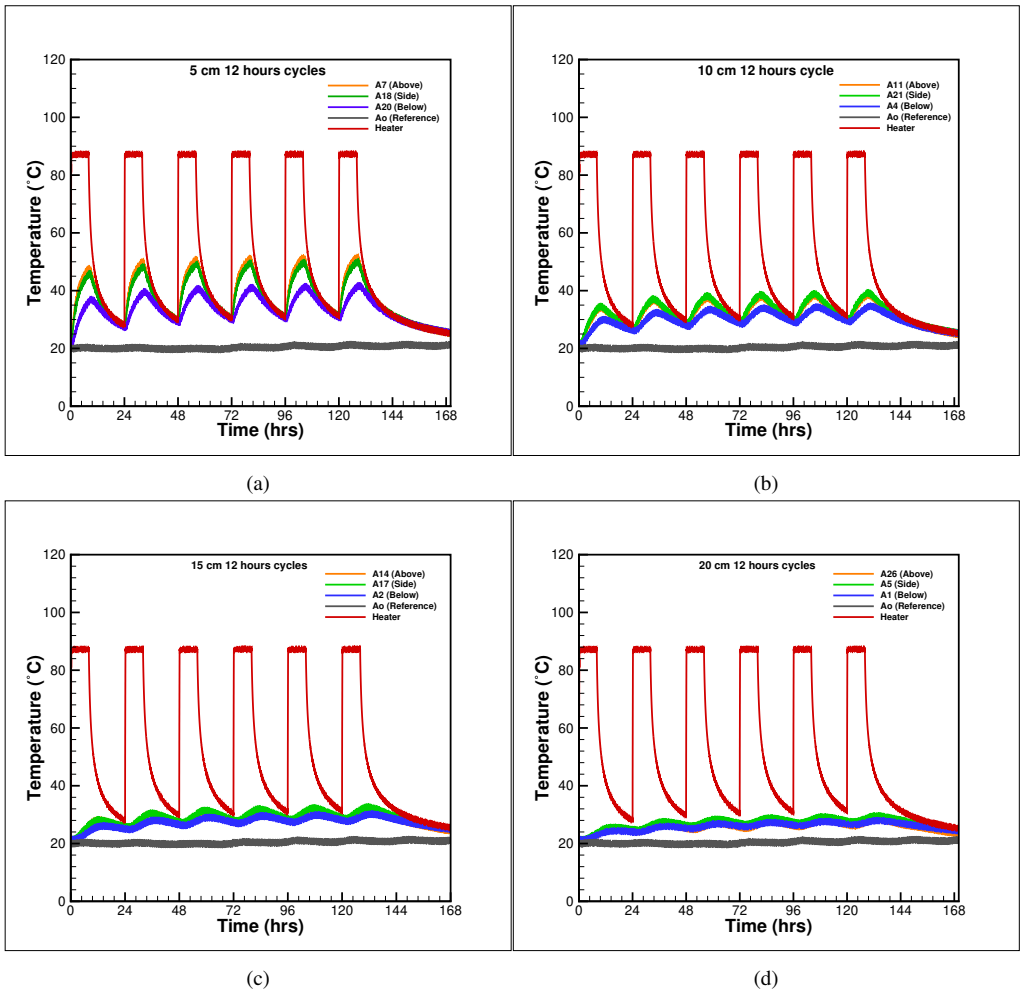

Fig. 5: The symmetrical heating-cooling cycle of 12 hours at a)5cm b)10cm c) 15cm d)20cm from the heater surface.

4.1.2 Unsymmetrical thermal heating-cooling cycles

The unsymmetrical loading tests are done with two thermal loading scenarios. The first test consists of three cycles of 1 hour of heating and 2 hours of cooling. The results show thermal charging taking place as well, but the intensity is lower than in the symmetrical case as more relaxation time is available for the system to dissipate heat into the surrounding (Fig. 6a-d). A general trend could be identified for the surrounding temperature behaviour near the heat source as a nonlinear fluctuating rise (6 a-b) for the TCs at 5 and 10 cm from the heater´s surface. However, the rise is linear for the far-field TCs, as observed in figure 6 (c-d) at 15 and 20 cm distance from the heater surface.

The second test is done with five cycles of 6 hours of heating and 18 hours of cooling (Fig. 7a-d). The results suggest that the TCs at 5cm distance from the heater surface reach a maximum value of 36.61 ^{o}C in the first cycle and 44.05 ^{o}C in the last cycle. The change is significant and the system fails to reach a static equilibrium with the surrounding sand. Compared to 12 hours of symmetric heating-cooling, a less sudden temperature rise is observed in Fig. 7d at the TC 20 cm away from the heater surface. The general trend is nonlinear and is similar to the near-field TCs recording. All the TCs show a nonlinear behaviour contrast to shorter heating-cooling cycles in figure (6 d), where the general trend for far-field TCs was observed as linear.

The dissimilarity arises due to the amount of energy given in the cases of 1 hour and 12 hours of heating. Both results from figure 6 and 7 show that the cooling time with unsymmetrical heating is also insufficient to prevent thermal charging of the sand. Therefore, two separate tests are performed with a longer relaxation time, and results are given in the following section.

4.1.3 Thermal relaxation time

To properly quantify the relaxation time to prevent thermal charging, two tests with 1 and 6 hours of heating and subsequent 23 and 36 hours of cooling are done (Fig. 8 and 9). The near-field TCs at 5 cm and 10 cm distances experience the switching

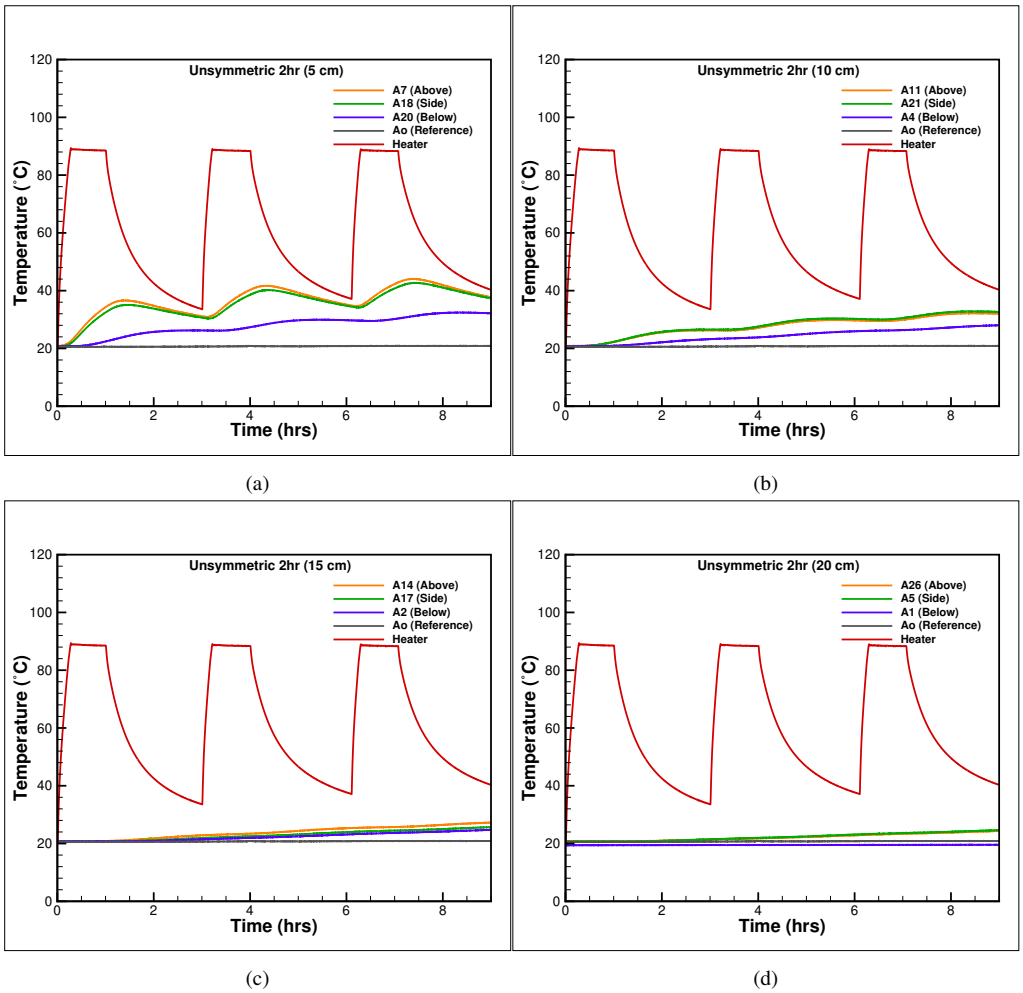

Fig. 6: The unsymmetrical 1 hour heating and 2 hours of cooling cycle at a)5cm b)10cm c) 15cm d)20cm from the heater surface.

off of the heater at once (Fig. 8 a-b), but the far-field temperature keeps on rising from the heat given by the heater during operation (Fig. 8 c-d). After 8 hours, the near-field TC as shown in Fig 8 (a,b) reaches equilibrium with the heater temperature, but the far-field TCs, 15 cm and 20 cm from the heater´s surface require 12 and 14 hours, respectively. The relaxation time of 23 hours is sufficient to bring the system close to the initial test temperature.

The test with 6 hours of heating and subsequent 36 hours of cooling is shown in Fig 9 (a-d). The longer heating time provides more energy and prolongs the relaxation time. The near-field TCs respond immediately with the heater switching off (Fig 9. a,b), but the far-field TCs continue recording the rising temperature as shown in Fig 9.d. At all the measurement points, the heater's temperature and the surrounding sand come to an equilibrium in an asymptotic fashion.

4.2 Static thermal loading test with dry and saturated sand

Two identical tests with dry and saturated sand are performed under similar loading boundary conditions. A comparison of the temperature difference between dry and fully saturated sand is plotted for four profiles around the heater ranging between 10 cm to 25 cm. The thermal buoyancy effect is observed at all measuring locations with all the four TCs above the heater, as shown in Fig. 10 (a-d). The thermocouples at equal distances from the heater´s surface show different behaviour and indicate the nonuniform heat transfer characteristics. The temperature difference graph shows a sizeable initial difference and subsequent drop in the difference value. The initial rise is due to higher thermal conductivity of saturated sand, which facilitates heat transfer. Soon after, a partial thermal equilibrium with the surrounding is established and the difference between dry and saturated condition reaches an asymptotic constant value (Fig. 10a-d).

The saturated sand shows a sharp rise of temperature above the heater after 72 hours of heating, and is visible at all thermocouples above the heater (Fig. 10a-d). The sudden increase of the temperature above the heater arises with the formation

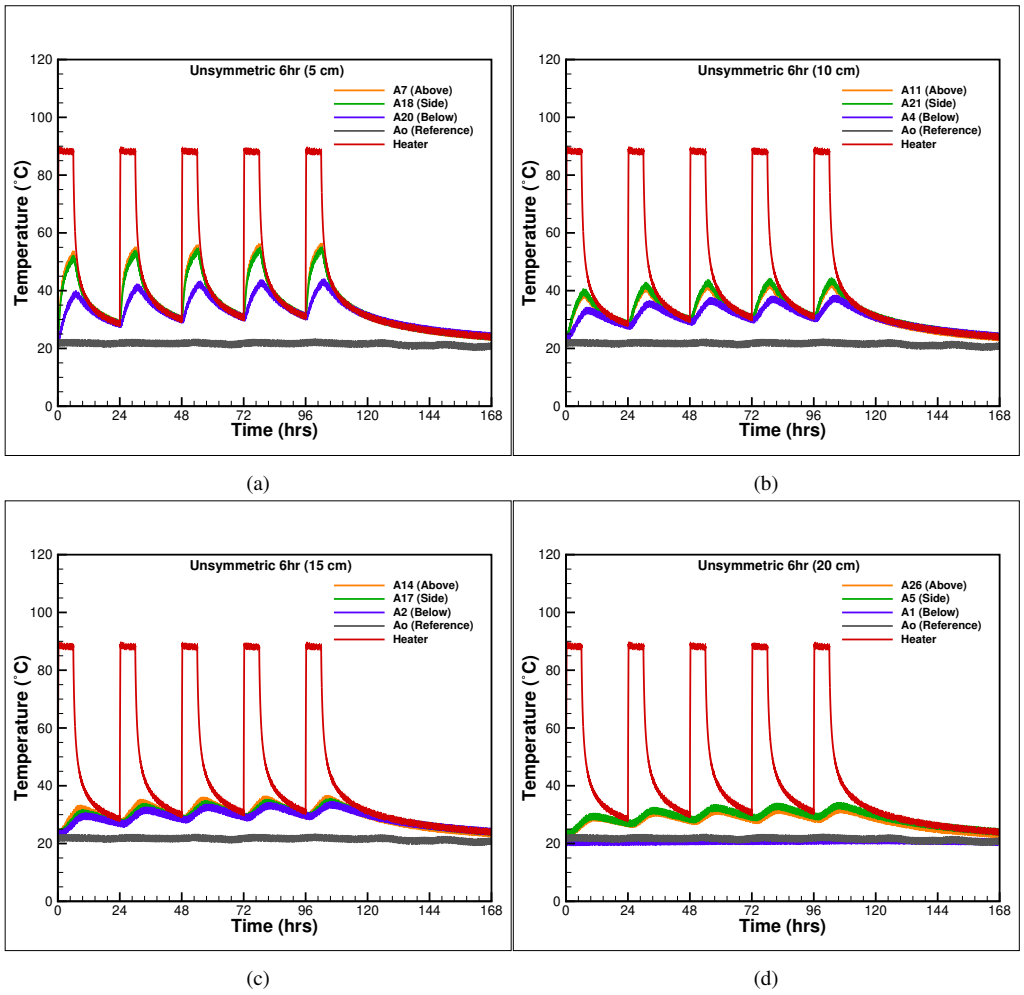

Fig. 7: The unsymmetrical heating of 6 - 18 hours cooling cycle of 1 hour at a)5cm b)10cm c) 15cm d)20cm from the heater surface.

of convection cells. No significant rise is observed in the horizontal plane and at the TCs below the heater. The convection heat transfer becomes dominant above the heater with increasing distance (Fig.10 a-d). The results indicate a density-driven buoyancy flow of liquid water and uneven channelised heating of the surrounding soil. Although channelised heating helps remove heat from the UGPS, it is undesirable under crop fields and causes damage to the plants' roots. The thermal buoyancy effect due to convective cells' formation has been previously reported for fully saturated porous media (35). It is shown that below a critical Reynolds number, convective cell flow is two dimensional and time-independent, but changes to time-dependent three-dimensional flow above the threshold, which depends inversely on the heater length and the burial depth. The burial depth of the UGPS is calculated from optimised trench construction costs, and ranges between 1.5-2.0 m to avoid damage from agricultural plugs and surface digging. Therefore, in the dimension reduced laboratory scaled model it is fixed at 45cm. The position of the heater is thus not varied and results in a two dimensional density-driven flow around the heater.

Fig. 11 shows the 2D temperature contour plot generated from the measured data for dry and fully saturated conditions. As measurements are performed only in half of the box, the symmetry condition is considered for full-field plotting. The cubic interpolation function is used to smooth the figure between measurement points. The contour plots offer better insight into the evolution of the convection cells for saturated sand around the heater with time.

Fig. 11 (a,c,e and g) and Fig. 11 (b,d,f and h) show the evolution of temperature in the dry and saturated conditions, respectively, after 3, 6, 9 and 120 hours of heating. The temperature near the heater reaches 70 °C and is shown with the colour bar. The temperature field in all dry condition is restricted in the vicinity of the heater and gradually increases as the time passes. For all the saturated sand tests, the temperature fields are broader and encompass a more significant area than the dry sand. Also, in Fig 11.h, which shows the temperature field after 120 hours, the thermal buoyancy is visible with a candle flame-like shape above the heater.

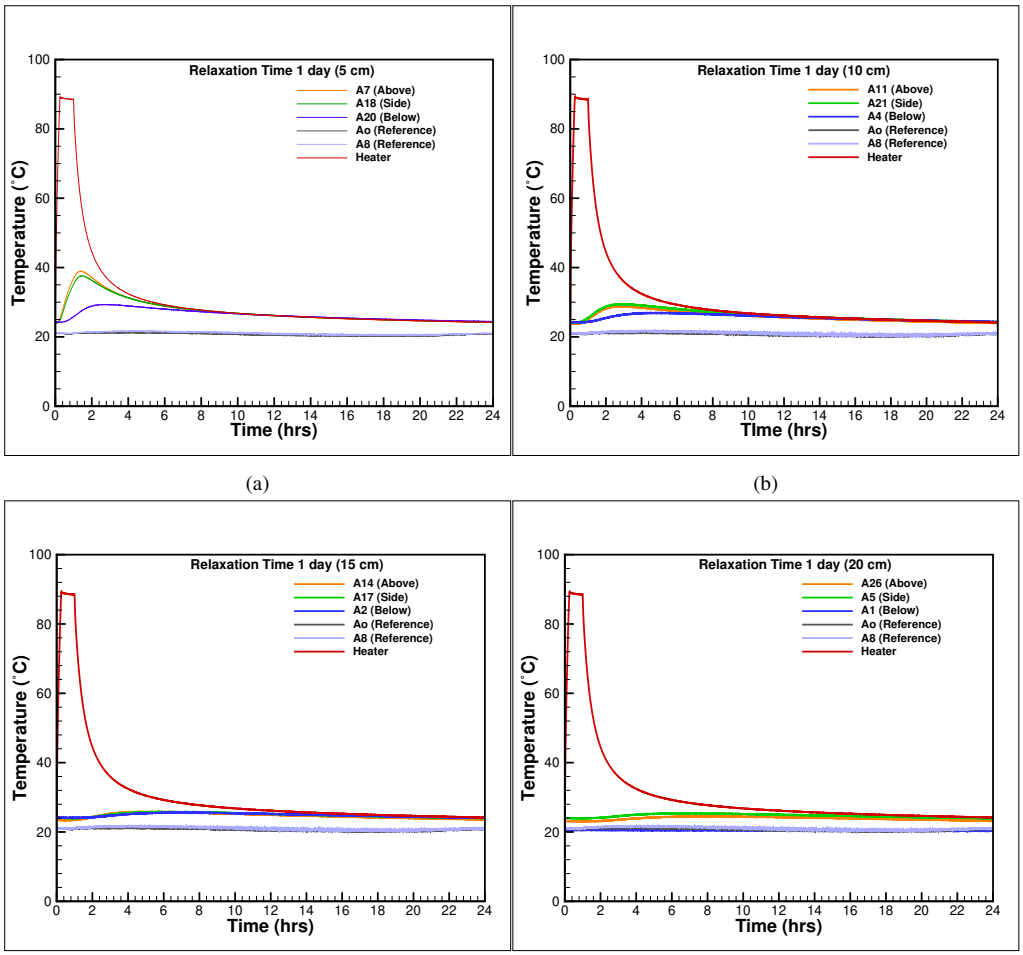

Fig. 8: The thermal relaxation time of 1 hour of heating and subsequent 23 hours of cooling at a)5cm b)10cm c) 15cm d)20cm from the heater surface.

The numerical and theoretical models for temperature field calculation around the UGPS do not consider the buoyancy effect, thus resulting in incorrect temperature distribution and heat loss computation. The channelised heat loss from the UGPS below a paddy crop field, at a crossing with the gas or water pipelines in high water table regions and near water bodies should be considered for correct temperature field calculation.

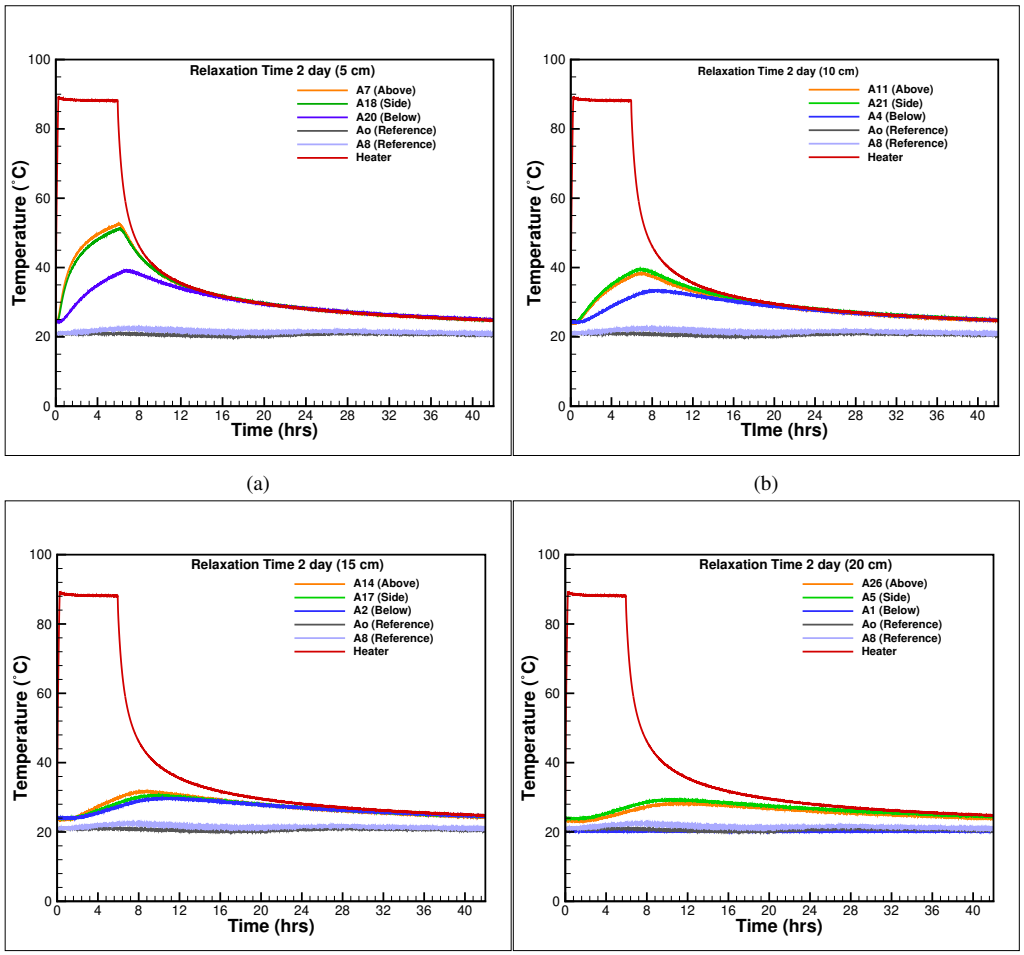

Fig. 9: The thermal relaxation time of 6 hours of heating and subsequent 36 hours of cooling at a)5 cm b)10 cm c) 15 cm d)20 cm from the heater surface.

5 Conclusion

In the paper, an experimental investigation is performed to assess the behaviour of dry and saturated sand around a heated cylinder representing an underground power cable system with cyclic and static thermal loading. The cyclic thermal loading with dry sand showed a significant thermal charging and reduction in the heat dissipation ability of the surrounding sand. The thermal relaxation tests with two different heating times of 1 and 6 hours showed asymptotic cooling of the sand. The static thermal loading tests with saturated sand show a significant density-driven convective heat transfer after 72 hours of heating. A comparison of heat transfer characteristics around the heater is shown with thermal contour maps drawn from experimental results for dry and saturated sand. The results show a buoyancy-driven convective heat transfer with saturated sand. The saturated sand improves the heat transfer capabilities but channelises it above the heater. The experimental results provide clear evidence for consideration of natural convection in calculating the temperature field and heat losses from an underground power cable system in high water table regions, near the water bodies and the crop fields.

Acknowledgements

Z. H. R. and F. W. would like to thank project DuoFill grant BMWi/KF3067303KI3 funded by Federal ministry for Energy, Germany. V.T. and S.I. thankfully acknowledged the support and funding provided by the Deanship of Scientific Research, King Khalid University, Abha, Kingdom of Saudi Arabia for the General Research Project under the grant number G.R.P./93/42.

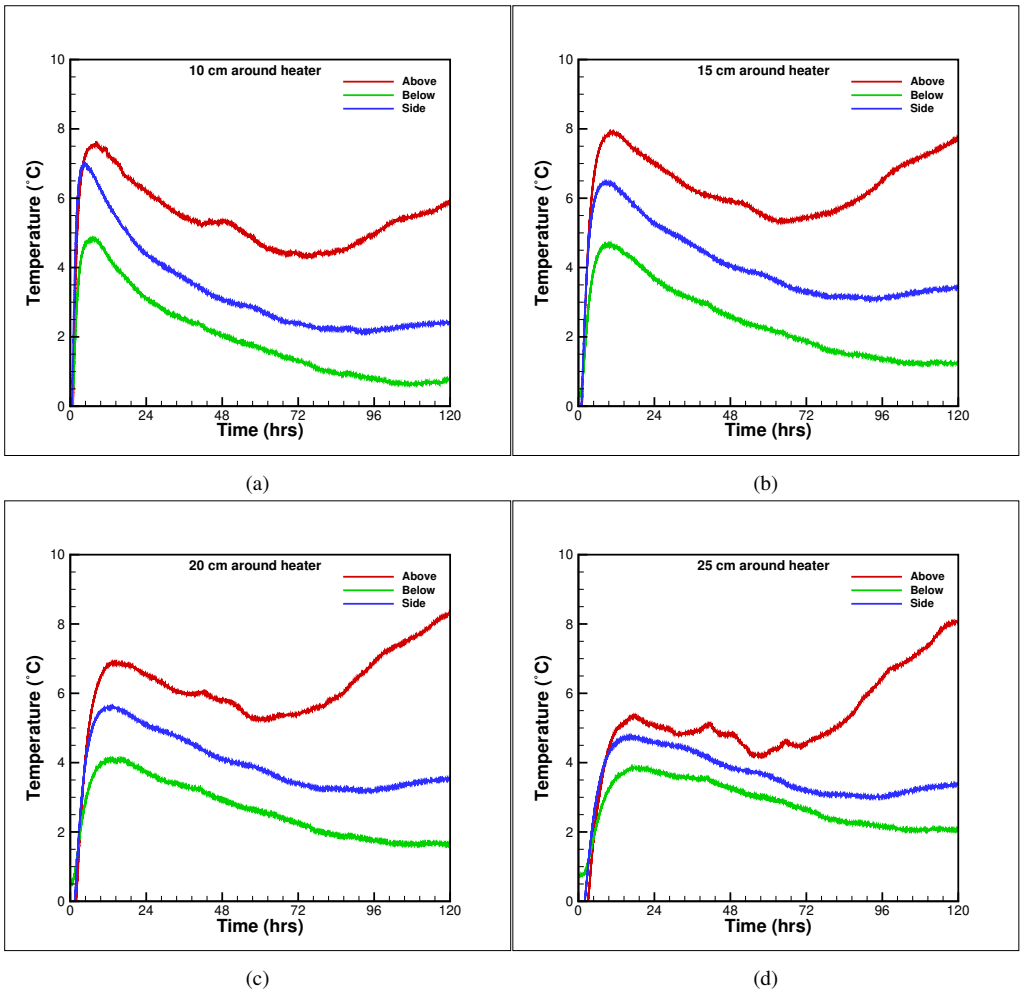

Fig. 10: Temperature differences around the heater between the dry and saturated soil conditions a)10 cm b)15 cm c) 20 cm d)25 cm from the heater surface.

Conflict of interest

The authors declare that they have no conflict of interest.

References

1. Francis, E.C., Shelley, O.P., Copper wire theft and high voltage electrical burns *International Journal of Burn & Trauma* **4(2)**59-61 (2014).
2. Van Dyke P., Havard D., Laneville A. Effect of Ice and Snow on the Dynamics of Transmission Line Conductors. *Atmospheric Icing of Power Networks* 171-228 (2008).
3. Shangzun, Y. Pengfei L. Ling, N. Study on Electromagnetic Radiation of Ultra-High Voltage Power Transmission Line, *International Conference on Computer Science and Information Technology*, 402-406 (2008).
4. Ahmad, S., Rizvi, Z.H., Khan, M.A., Ahmad, J., Wuttke, F. Experimental study of thermal performance of the backfill material around underground power cable under steady and cyclic thermal loading *Materials today: proceedings* **17:1** 85-95 (2019).
5. Oclon, P., Pobedza, J., Walczak, P., Cisek, P., and Vallati, A. Experimental Validation of a Heat Transfer Model in Underground Power Cable Systems. Energies, Multidisciplinary Digital Publishing Institute, 13(7), 1747 (2020).
6. International Standard IEC 60287-2-1, Electric Cables - Calculation of the current rating - Part 2-1: Thermal resistance - Calculation of the thermal resistance
7. IEEE Std 835-1994 Standard Power Cable Ampacity Tables

8. Al-Saud, M. S., El-Kady, M. A., and Findlay, R. D., A new approach to underground cable performance assessment. *Electric Power Systems Research***78(5)**, 907–918 (2008).
9. Neher, J.H., McGrath, M.H., The calculation of the temperature rise and load capability of cable systems, *AIEE Transactions***Part**3 (1957).
10. Sellers, S.M., Black, W.Z., Refinements to the Neher-McGrath model for calculating the ampacity of underground cables, *IEEE Transactions on Power Delivery***11** (1996).
11. de Lieto Vollaro, R., Fontana, L., Vallati, A., Thermal analysis of underground electrical power cables buried in non-homogeneous soils *Applied Thermal Engineering***31** 772-778 (2011).
12. Ocłoń, P., Rerak, M., Rao, R. V., Cisek, P., Vallati, A., Jakubek, D., and Rozegnał, B. "Multiobjective optimization of underground power cable systems." Energy, 215, 119089 (2021).
13. Calcara, L., Sangiovanni, S., and Pompili, M. (2017). "MV underground cables: Effects of soil thermal resistivity on anomalous working temperatures." AEIT International Annual Conference, 1–5 (2017).
14. Gouda, O. E., Osman, G. F. A., Salem, W. A. A., and Arafa, S. H. "Cyclic Loading of Underground Cables Including the Variations of Backfill Soil Thermal Resistivity and Specific Heat With Temperature Variation." IEEE Transactions on Power Delivery, 33(6), 3122–3129 (2018).
15. Salata, F., Nardecchia, F., Gugliermetti, F., and de Lieto Vollaro, A. "How thermal conductivity of excavation materials affects the behavior of underground power cables." Applied Thermal Engineering, 100, 528–537 (2016).
16. de Leon, F., Anders, G.J., Effects of backfilling on cable ampacity analyzed with the finite elements method, *IEEE Transactions on Power Delivery***23**, 537-543 (2008).
17. Wiecek, B., De Mey, G., Chatziathanasiou,V., Papagiannakis, A.,Theodosoglou, I. Harmonic analysis of dynamic thermal problems in high voltage overhead transmission lines and buried cables. Electrical Power and Energy Systems 58 199–205 (2014).
18. Rasoulpoor, M. Mirzaie, M. Mirimani, S.M. Thermal assessment of sheathed medium voltage power cables under non-sinusoidal current and daily load cycle. Applied Thermal Engineering, 123, 353–64 (2017).
19. Groeneveld, G. J., Snijders,A. L., Koopmans G., Vermeer, J. Improved method to calculate the critical conditions for drying out sandy soils around power cables. *IEE Proceedings C (Generation, Transmission and Distribution)* **131**(2), 42 – 53 (1984).
20. Ainhirn, F., Woschitz, R., Bolzer, A. Extended Approach for Calculating Thermal Stress and Ampacity of High Voltage Cable Systems Based on Experimental Data *Jicable'19 - 10th International Conference on Insulated Power Cables* (2019).
21. Snijders, A. L. Groeneveld, G. J. Vermeer, J. van de Wiel, G., M. L. M. Report presented at Workshop Current Rating of Buried Cables in Relation to Thermal Properties of Soil (1984).
22. Trinks, L.K.,Einfluss des Wasser- und Wärmehaushaltes von Böden auf den Betrieb erdverlegter Energiekabel *PhD thesis* Technical University Berlin (2010) (In German).
23. F. Ainhirn, Environmental Parameter Modelling for Thermal Rating Calculations of Power Cables in Urban Areas using Machine Learning and Big Data, *2020 IEEE International Smart Cities Conference (ISC2)*, Piscataway, NJ, USA, 1-7,(2020).
24. de Lieto Vollaro, R., Fontana, L., Vallati, A., Experimental study of thermal field deriving from an underground electrical power cable buried in non-homogeneous soils, *Applied Thermal Engineering***62**, 390-397 (2014).
25. Hartley, J. G., and Black, W. Z. "Transient Simultaneous Heat and Mass Transfer in Moist, Unsaturated Soils." Journal of Heat Transfer, American Society of Mechanical Engineers Digital Collection, 103(2), 376–382 (1981).
26. Chatzipanagiotou, P., Chatziathanasiou, V., de Mey, G., Wiecek, B., Influence of soil humidity on the thermal impedance, time constant and structure function of underground cables: A laboratory experiment *Applied Thermal Engineering***113**, 1444–1451 (2017).
27. Moya, R.E.S., Prata, A.T., Cunha Neto, J.A.B., Experimental analysis of unsteady heat and moisture transfer around a heated cylinder buried into a porous medium, *International Journal of Heat and Mass Transfer* **31**, 1076-1087 (1999).
28. Salata, F. Nardecchia, F. de Lieto Vollaro, A. Gugliermetti, F. Underground electric cables a correct evaluation of the soil thermal resistance. Applied Thermal Engineering, 78, 268–77 (2015).
29. Oclon, P., Pobedza, J., Walczak, P., Cisek, P., and Vallati, A. "Experimental Validation of a Heat Transfer Model in Underground Power Cable Systems." Energies, Multidisciplinary Digital Publishing Institute, 13(7), 1747.(2020).
30. Jury, W.A., Simultaneous transport of heat and moisture through a medium sand, *Ph.D. Thesis*, University of Wisconsin (1973).
31. Philip, J.R., de Vries, D.A. Moisture Movement in Porous Materials under Temperature Gradients *Transactions American Geophysical Union* **38** (2) 222-232 (1957).
32. de Vries, D.A. The theory of heat and moisture transfer in porous media revisited *International Journal of Heat and Mass Transfer* **30** (7) 1343-1350 (1987).
33. Kroener, E., Vallati, A., and Bittelli, M. Numerical simulation of coupled heat, liquid water and water vapor in soils for heat dissipation of underground electrical power cables. *Applied Thermal Engineering* **70(1)**, 510–523 (2014).
34. Hruska, M., C. Clauser, and R.W. De Doncker. The effect of drying around power cables on the vadose zone temperature. *Vadose Zone J.* **17** 180105 (2018).

35. Himasekhar, K., Bau, H.H. Thermal Convection Around a Heat Source Embedded in a Box Containing a Saturated Porous Medium *Journal of Heat Transfer* **110**(3), 649-654 (1988).

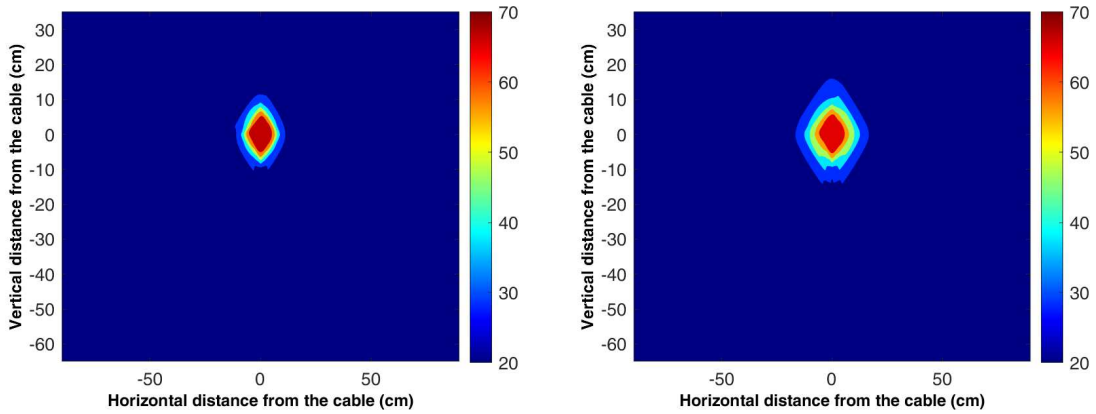

(a) Dry after 3 hours

(b) Saturated after 3 hours

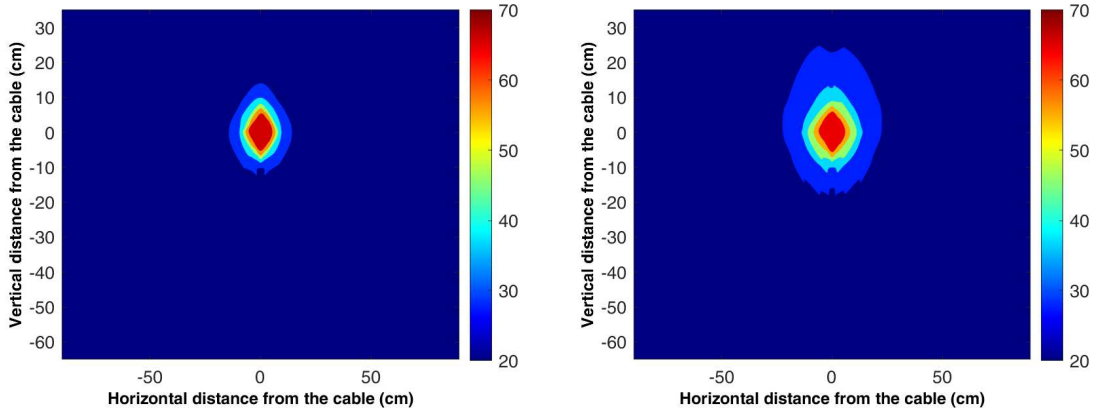

(c) Dry after 6 hours

(d) Saturated after 6 hours

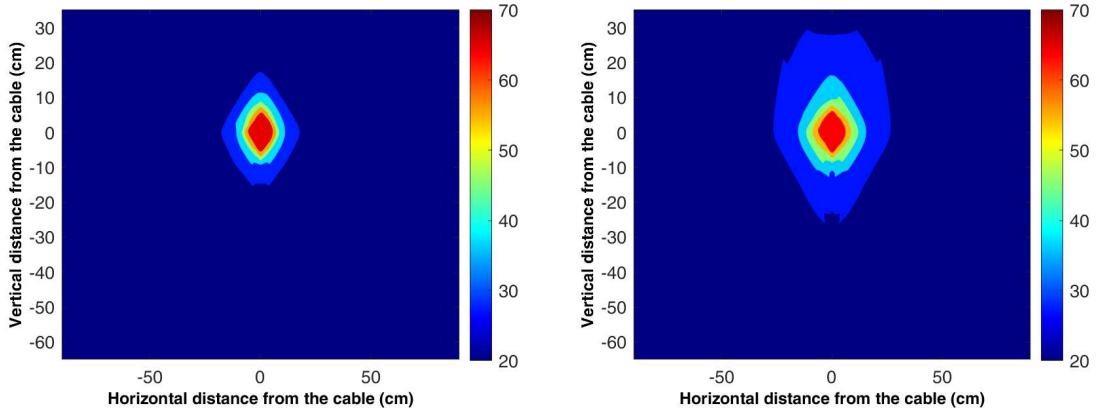

(e) Dry after 12 hours

(f) Saturated after 12 hours

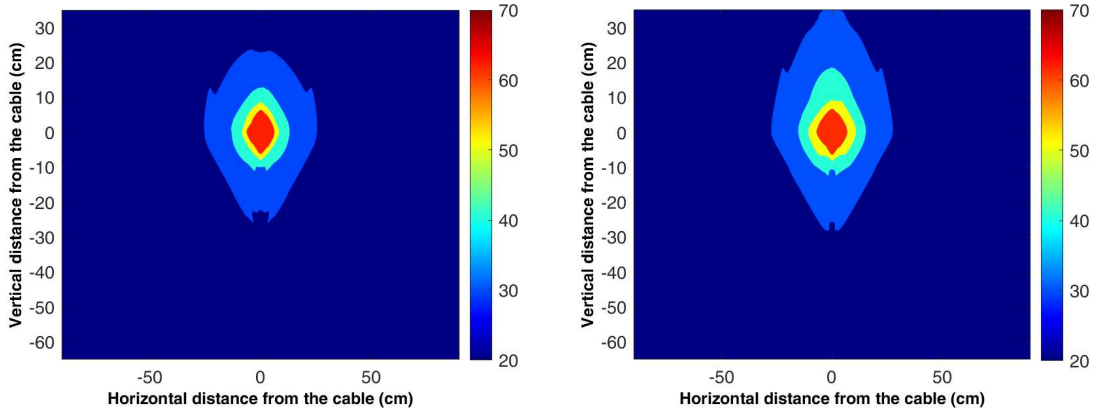

(g) Dry after 120 hours

(h) Saturated after 120 hours

Fig. 11: Experimental contour plots for the evolution of temperature in the box in dry and saturated condition after 3, 6, 12 and 120 hours. The left side figures are for dry and the right are for fully saturated sand.